Raman imaging demonstrates FGF2-induced craniosynostosis in mouse calvaria

Nicole J. Crane
Michael D. Morris
The University of Michigan
Department of Chemistry
Ann Arbor, Michigan 48109-1055

Michael A. Ignelzi, Jr.
Genggeng Yu
The University of Michigan School of Dentistry
Department of Orthodontics and Pediatric Dentistry
Ann Arbor, Michigan 48109-1078

Abstract. Craniosynostosis is a severe craniofacial disease where one or more sutures, the fibrous tissue that lies between the cranial bones, fuses prematurely. Some craniosynostosis syndromes are known to be caused by mutations in fibroblast growth factor (FGF) receptors. Mutated FGF receptors are thought to cause constitutive signaling. In this study, heparin acrylic beads released fibroblast growth factor 2 (FGF2) to mimic constitutive signaling by mutated receptors, delivering FGF2 in addition to already existing normal tissue amounts. Fetal day 18.5 mouse sutures were treated with FGF2-soaked beads and cultured in serum free media for 48 h. We have shown previously that this treatment leads to fusion and increased Msx2 expression, but here we use near-infrared Raman imaging to simultaneously examine the mineral components and matrix components of cranial tissue while providing light microscopic spatial information. FGF2-treated mouse sutures show increased v_1 phosphate and v_1 carbonate bandwidths, indicating a slightly chemically modified mineral being rapidly deposited. In addition, FGF2-treated mouse sutures show a marked increase in mineral-to-matrix ratios compared to control mouse sutures, typical of increased mineralization. © *2005 Society of Photo-Optical Instrumentation Engineers.* [DOI: 10.1117/1.1908057]

Keywords: Raman imaging; bone; mineralization; mouse; craniosynostosis; fibroblast; growth factors.

Paper 04096R received Jun. 8, 2004; revised manuscript received Sep. 1, 2004; accepted for publication Sep. 13, 2004; published online May 24, 2005.

1 Introduction

Craniosynostosis is the second most common craniofacial birth defect, affecting 1 in 2400 live births.[1,2] It occurs as a part of more than 150 syndromes, including Saethre–Chotzen, Apert, Pfieffer and Carpenter's syndrome and Crouzon's disease.[3] Craniosynostosis causes premature fusion of the sutures, the fibrous tissue that lies between the cranial bones. Presently, the only method to treat affected children is to surgically cut the fused sutures to allow proper cranial growth, often before two months of age.[4]

Unlike many other bones in the body, the skull undergoes only one type of mineralization, intramembranous ossification.[5] Davies presents a three-step process for biological calcification. In the first step, organic matrix (primarily collagen) is secreted and deposited. Next, the matrix is modified so that it can become mineralized and finally the matrix is mineralized.[6] The bone growth sites in intramembranous ossification need to remain unmineralized yet allow for new bone to grow at overlapping osteogenic fronts. Mesenchymal cells within the suture remain undifferentiated while osteoblasts, the new bone cells, are enlisted to the osteogenic fronts. The osteoblasts form the osteoid on the osteogenic front and eventually mineralize to form new bone (Fig. 1). When this process goes awry and the bone growth sites, or

sutures, ossify, craniosynostosis is the result. Craniosynostosis effectively prevents the cranial plates from moving apart to allow for neurocranial growth.[7]

Craniosynostosis is caused by genetic mutations.[8] Mutations in the following human genes have been identified and associated with craniosynostosis: MSX2, FGFR1-3, and TWIST.[9–11] These genetic defects have been shown to cause an increase in the number of osteogenic precursor cells (preosteoblasts and osteoblasts) and an increase in nonmineralized and mineralized matrix production.[12,13] Osteoblasts are bone-forming cells that produce and export collagen as well as some other matrix molecules.[14] These studies also show sutural fusion as a result of craniosynostosis caused by the genetic mutations.[12,15] Greenwald et al. used replication-deficient adenoviruses encoded with fibroblast growth factor 2 (FGF2) to increase FGF2 biological activity in coronal sutures and then cultured the sutures for 30 days. As a result, the coronal sutures fused, thereby demonstrating the morphology of unilateral coronal synostosis.[16] Similarly, FGF2-treated posterior frontal sutures in rats show enhanced suture fusion.[17]

In this study we increased the FGF2 concentration in the suture region to mimic activated signaling by mutated FGF2 receptors. We have shown that fetal mouse sutures treated with FGF2-soaked acrylic beads leads to increased Msx2 ex-

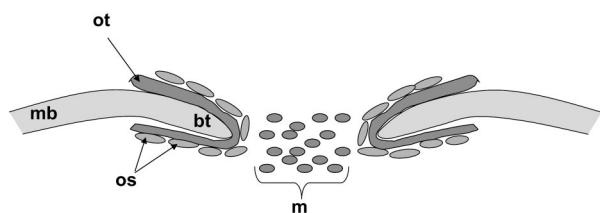Address all correspondence to Michael D. Morris. Tel: 734-764-7360; Fax: 734-615-3790; E-mail: mdmorris@umich.edu

Fig. 1 Diagram of intramembranous ossification for a patent suture, i.e., sagittal suture; mb=mature bone, ot=osteoid, os=osteoblast, bt=bone tip, and m=mesenchymal cells.

pression along with suture obliteration and fusion. When compared to other sutures, the coronal suture had an overall greater response to the FGF2 soaked beads.[18] The purpose of this study was to explore possible chemical changes within the bone tissue resulting from the FGF2-induced craniosynostotic tissue.

Raman spectroscopy offers important advantages for examining delicate tissues containing large amounts of water such as murine calvaria. Like Fourier transform infrared (FTIR) spectroscopy, Raman spectroscopy provides conclusive chemical structure identification of the major components of the tissue. In this sense vibrational spectroscopic identification is complementary to methods such as scanning electron microscopy and atomic force microscopy. These technologies provide images with exquisite morphological detail but very limited chemical structure information. Raman and FTIR spectroscopies are especially useful in the study of mineralized tissues because both provide simultaneous information on the mineral and matrix. Moreover, they illuminate subtle compositional differences such as the state of matrix interfibril cross-links and mineral crystallinity.[19–31]

Unambiguous detailed compositional information is an advantage of spectroscopy over many familiar histological stains. On the other hand, the established staining methodologies require no specialized instrumentation and are therefore widely available. The limitations of von Kossa staining, for example, have recently been demonstrated.[32] While von Kossa staining is often used to identify mineral content in tissue sections it does not do so unambiguously. Silver ion reacts with any inorganic phosphate in an acidic environment, regardless of its biological or inorganic origin.[33] Similarly, although stains like Alizarin red bind specifically to calcium, any calcium-binding proteins or proteoglycans in the tissue can produce false positive results. In bone tissue it is reasonable to assume that collagen is a major component and that eosin staining visualizes collagen. But eosin cannot report on secondary structure or collagen cross-linking, known strengths of both FTIR and Raman spectroscopy.

For our application Raman spectroscopy offers certain advantages over the more familiar FTIR. Because Raman spectroscopy is a scattering technique, the specimens need not be thin. Indeed, intact bone specimens can be examined. Raman spectroscopy offers resolution similar to that of light microscopy. With the near-infrared lasers used in our laboratory, typical lateral resolution is about $2–3$ μm and 0.5 μm is available with high numerical aperture (NA) immersion objectives. The Raman bands of water do not interfere spectroscopically with other Raman bands of interest, while the water

bands in FTIR often obscure important protein information. With few exceptions Raman spectroscopy is compatible with standard histological stains and previously stained specimens can be examined spectroscopically.[34] In this study we use Raman near-infrared imaging to examine the mineral and matrix composition of normal and craniosynostotic sections of fetal day 18.5 mouse calvaria.

2 Materials and Methods

2.1 Specimen Preparation

Twenty-eight B6CBA F_1/J wild-type mice were harvested at fetal day 18.5 and prepared as described.[18] Briefly, calvaria, the topmost bones of the skull, were excised and placed in serum-free media containing DMEM, 1 μ/mL gentamicin, 2 mM glutamine, 1 mM nonessential amino acids, 1 mM ITS+ (BD Biosciences, Bedford, MA) and 3 mM inorganic phosphate. Eight to ten $200–250$ μm heparin acrylic beads (Sigma Aldrich Corporation, St. Louis, MO) soaked with recombinant human FGF2 were placed evenly along the sutures of nine calvaria. Empty beads were used as controls for nine calvaria and ten calvaria received no bead treatment. Following the 48 h culture period, calvaria were rinsed twice with phosphate buffered saline at pH 7.2. Next, the specimens were subjected to controlled dehydration: 100% ethanol for 30 min, 85% ethanol for 30 min, and 70% ethanol for 30 min. Dehydrated specimens were refrigerated and stored in 70% ethanol. Individual sutures were isolated and embedded in glycol methacrylate (Energy Beam Sciences, Wigam, MA), $15–20$ μm sections were made with a JB-4 microtome (Energy Beam Sciences, Wigam, MA) using glass knives. Sections were then mounted onto Probe-On-Plus microscope slides (Fisher Scientific, Pittsburgh, PA) and allowed to air dry. For mineral confirmation, sections were stained with Alizarin red.

2.2 Raman Spectroscopy

Microscope slides were placed under a modified epifluorescence microscope (Olympus, Inc., Melville, NY; BH-2) onto a motorized X-Y stage (NEAT, Salem, NH) where a line-focused 785 nm laser (Kaiser Optical Systems Inc., 400 mW output) was focused onto the specimen through a $10\times/0.5$ NA Fluar objective (Zeiss, Thornwood, NY) producing incident laser power of $\sim$250 mW. Raman scatter was collected through the same objective and focused into an axial-transmissive spectrograph (Kaiser Optical Systems Inc., Ann Arbor, MI; Holospec f/1.8I) equipped with a 25 μm slit, providing spectral resolution of $3–4$ cm^{-1}. Signal detection was achieved with a back-thinned, deep depletion, thermoelectrically cooled charge coupled device camera (Andor Technology, South Windsor, CT). A spectrum contains 1024 spectral elements spanning the Raman shift range of $\sim$200–2000 cm^{-1}.

One hundred lines of Raman spectra spaced 1.3 μm apart (2.6 μm spatial resolution) were acquired to provide approximately 360×130 (H$\times$W) μm images. Each line consisted of 254 Raman spectra spaced 1.3 μm apart. Total acquisition time for each section was approximately 5 h. Four to six sections of coronal and sagittal sutures were examined for each treatment group for a total of 28 examined sections.

2.3 Data Analysis

For all spectroscopic data sets multivariate analyses were carried out in MATLAB (MathWorks, Inc., Natick, MA) using vendor and locally written scripts. All spectra were corrected for dark current. The analysis procedure began with principal component analysis (PCA) which has been previously described.[19,34]

To maximize signal/noise ratio in the data recovered by PCA, extraction of Raman spectra was performed by band target entropy minimization (BTEM).[35] BTEM is based on the information entropy minimization concept which was introduced into the life sciences by Sasaki, Kawata, and Minami as a method for processing images obtained by multispectral fluorescence microscopy.[36] Widjaja and co-workers developed this technique as a method for extracting individual chemical component infrared spectra from sets of spectra of component mixtures.[37] These workers also introduced the BTEM nomenclature. BTEM has been modified by our laboratory as a method to extract Raman spectra and Raman images from Raman imaging microscopy data sets. We have shown that as a Raman image processing method, BTEM offers higher signal/noise ratio than previously published methods and can sometimes recover component spectra that are not recovered by other methods.[35] BTEM also provides results that are less subjective than standard PCA manual rotation. In addition, BTEM requires considerably less execution time than PCA manual rotation.

The first step in BTEM is PCA. Rather than taking sums and differences of the first few eigenvectors, BTEM targets user-chosen spectral features that are observed in these eigenvectors. The next step is a constrained rotation of eigenvectors to extract a Raman spectrum. The rotation is not limited to those eigenvectors that are clearly nonnoise eigenvectors. Instead, the next 10–50 additional eigenvectors that contain small amounts of information are included in the rotation. An entropy minimization criterion or a closely related mathematical function is used in addition to a non-negativity constraint to obtain a representation of a Raman spectrum. Criteria for determining how many eigenvectors to include are used to avoid overfitting. The resulting vectors are called factors and are non-negative. The relative intensities (scores) are proportional to the relative chemical component amounts. The spatial distribution of these scores is plotted as the Raman images of tissue components. In this manuscript only bone tissue Raman factors and score images are reported. Descriptions of residual background luminescence and the Raman factor and image of the embedding medium glycolmethacrylate (GMA) are not shown. The GMA factor displays prominent Raman bands at 827, 853, 894, 967, 1026, and 1090 cm^{-1}. The score images show that the GMA intensity is least where the mineral factor intensity is greatest. The mathematical separation of GMA signal from bone tissue signal has been discussed in detail elsewhere.[34]

All factors were base line corrected with a cubic or quartic function. To ensure that the score images are consistent with individual factor intensity, the mineral score area was multiplied by the area of the corresponding mineral factor phosphate band at 958 cm^{-1}. Similarly, the matrix score image was multiplied by the sum of the areas of three matrix factor bands at 856 cm^{-1} (hydroxyproline), 876 cm^{-1} (hydroxypro-
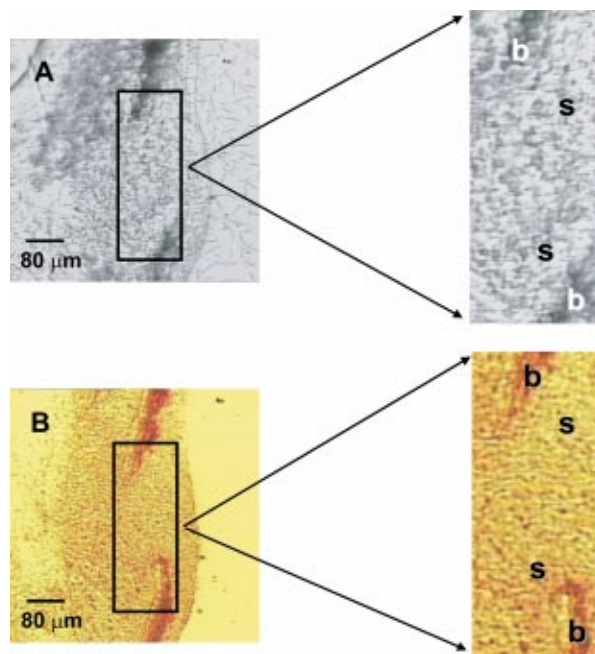

Fig. 2 Bright field image of a section of the sagittal suture and surrounding bone unstained (A) and stained with Alizarin red (B). The box indicates the imaged region of the section; b signifies a bone region and s signifies a suture region. Scale bar on bright field images is 80 μm. The inset dimensions are ~360 μm×~130 μm (H×W).

line), and 921 cm^{-1} (proline).[38] This effectively intensity normalizes the score images so that the mineral-to-matrix ratios (MTMRs) can be compared. These bands were chosen because type I collagen is composed of ~11% hydroxyproline and ~13% proline.[39] These amino acids comprise nearly constant percentages of bone matrix. Additionally the intensities and positions of these bands are less sensitive to changes in collagen secondary structure than amide backbone vibrations. Other workers have used the amide I band area[29] at 1660 cm^{-1} or CH$_2$ wag area[40] at 1450 cm^{-1} as markers of matrix content.[41] The spectroscopic MTMRs are then calculated by dividing the normalized mineral score image by the normalized matrix score image. Nine adjacent points within the MTMR score images were used to determine bone region and suture region MTMR averages and standard deviations.

Bandwidth measurements were made on the factors themselves. The recovered factors ride on a small amount of background that was removed by fitting background-only regions of the spectrum to a cubic or quartic function and subtracting. Background subtraction and fitting of the Raman bands was performed in Grams/AI (Thermo Galactic, Inc., Salem, NH). The fitted peaks were mixed Gaussian and Lorentzian functions. Peaks were not considered fitted until the solution converged with an R^2 value of 0.99 or greater. A two-tailed t test with unequal variances was performed to determine differences between the averages of the three conditions. Differences were considered significant with $p \leqslant 0.05$.

3 Results

A calvarial section, typical of those examined, is shown in Figs. 2(A) and 2(B). Bone regions consist of dense tissue and appear darker in color, while the suture appears only slightly

Table 1 Assignments for the Raman bands of the tissue components (see Refs. 26, 38, 41, 46, 47).

Raman shift (cm^{-1})	Band assignment	Component
826	v(CC) of backbone	Collagen
851	v(CC) of hydroxyproline ring	Collagen
876	v(CC) of hydroxyproline ring	Collagen
917	v(CC) of proline ring	Collagen
945	v_1 PO$_4$ stretch	Disordered calcium phosphate
959	v_1 PO$_4$ stretch	Stoichiometric carbonated hydroxyapatite
1001	Phenylalanine	Collagen
1070–1077	$v_1(CO_3^{2-})$	B-type carbonated hydroxyapatite

darker than the GMA. Mineral regions are defined as those bearing the deep red color of Alizarin red staining in Fig. 2(B). Alizarin red is a calcium binding stain, forming orange-red lakes with the calcium present in tissues such as bone. The region between the two bone tips is the suture proper. Most images consist of two bone tips. Two points within the suture proper were examined when possible.

3.1 Data Analysis

For no bead, empty bead and FGF2-treated sutures, BTEM yielded only two tissue Raman factors. One was a mineral factor and the other a collagenous matrix factor. The Raman bands of interest are listed in Table 1. The mineral factor [Fig. 3(A)] contains the intense v_1 PO$_4^{3-}$ 958 cm^{-1} band along with a band resulting from the overlapping v_1 CO$_3^{2-}$ band and the v_3 PO$_4^{3-}$ band at 1070–1075 cm^{-1}. Both bands are typical of a lightly *B*-type carbonated apatite. A matrix factor [Fig. 3(C)] was found for no bead, empty bead and FGF2-treated sutures. The Raman bands are those of immature bone matrix and consist primarily of type I collagen bands for hydroxyproline, proline and phenylalanine (851, 876, 917, and 1001 cm^{-1}, respectively). In earlier studies we were also able to recover only one mineral factor for fetal day 18.5 mouse calvarial tissue, although two mineral factors were recovered from postnatal day 1 tissue.[19]

The mineral score image [Fig. 3(B)] correlates well with the bright field image of the examined region. The most intense regions (red and yellow) correspond to the heavily mineralized bone tips while the blue region in the center correlates to the suture proper. The matrix score image is shown in Fig. 3(D). Separate mineral and matrix factors are recovered because the mineral is deposited onto a scaffold of collagen. Consequently, the spatial variation of matrix need not be the same as that of mineral.

3.2 Mineral-to-Matrix Ratios

The MTMRs representative of no bead, empty bead and FGF2-treated specimens are plotted in Fig. 4. It is expected that the MTMR in the bone tips will be much greater than that in the suture region. For the control specimens, no bead [Fig. 4(A)] and empty bead [Fig. 4(B)], the MTMRs do not

vary significantly between bone and suture regions ($p > 0.20$). However, the MTMRs for FGF2-treated specimens reveal a significant ($p < 0.01$) and large difference between the bone and suture regions. The data are summarized in graphical form in Fig. 5. This significant difference is seen in both the coronal [Fig. 5(A)] and sagittal sutures [Fig. 5(B)].

3.3 Bandwidth Comparison

Figure 6 shows a mineral factor that is curve fitted with mixed Gaussian and Lorentzian shaped bands. The v_1 PO$_4^{3-}$ band in
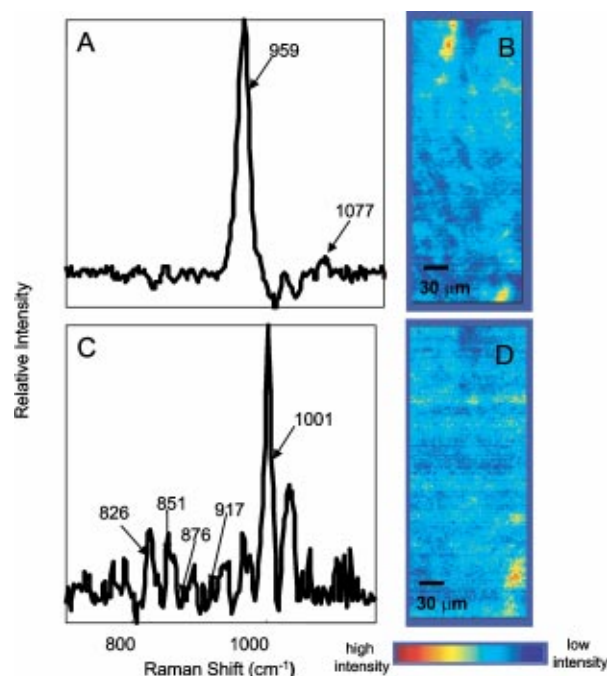

Fig. 3 BTEM reveals a single mineral and matrix factor, A and C respectively. The mineral factor (A) is denoted by the v_1 PO$_4^{3-}$ stretch at 958 cm^{-1} and the v_1 CO$_3^{2-}$ stretch at 1077 cm^{-1}. The matrix factor (C) is dominated by collagen bands. All other factors (GMA, glass, background luminescence) have been omitted for clarity. The corresponding score images show the spatial variation of the mineral (B) and matrix (D). Scale bar=30 μm. The score image dimensions are $\sim$360 μm$\times\sim$130 μm (H$\times$W).
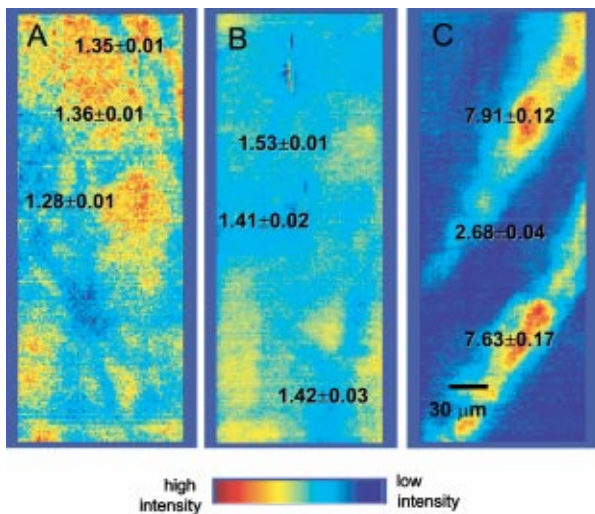
Fig. 4 Mineral-to-matrix ratio (MTMR) images indicate the MTMR for bone and suture regions for a no bead, empty bead and FGF2 soaked bead (A, B and C, respectively) coronal suture. In all images the center MTMR is a representation of the suture region while the remaining MTMRs correspond to bone regions. Note the relatively uniform distribution of the MTMR in the no bead (A) and empty bead (B) coronal sutures compared to the increased MTMR of the bone regions treated with FGF2 (C). Scale bar=30 μm. The MTMR image dimensions are $\sim$360 μm$\times\sim$130 μm (H$\times$W).

Fig. 5 The mean MTMR for the FGF2-treated bone region adjacent to the coronal suture (A) is significantly greater than that of the no bead or empty bead bone regions adjacent to the coronal sutures while the mean MTMR of the suture region for the no bead, empty bead and FGF2-treated coronal sutures shows no significant differences. Similar results were found for the sagittal sutures (B). The asterisks indicate $p < 0.01$.

bone mineral is asymmetric because the band actually consists of two or three closely spaced and unresolved bands. To best model this band, two underlying bands are used, 945, and 958 cm^{-1}. The carbonate band at 1071 cm^{-1} is less asymmetric and fitted with a single band.

We examined the mineral bands of the coronal [Fig. 7(A)] and sagittal [Fig. 7(B)] suture bone regions for differences in bandwidths. Changes in bandwidth are indicative of chemical changes in the mineral composition, including changes in total crystal lattice order. There is no significant difference ($p > 0.15$) in widths of the 958 cm^{-1} band between no bead, empty bead and FGF2-treated specimens. In all cases they are 8 cm^{-1} [full width at half maximum (FWHM) height]. For the 1071 cm^{-1} band, the FGF2-treated soaked specimens have a wider bandwidth (FWHM=$\sim$7 cm^{-1} for coronal specimens and $\sim$9 cm^{-1} for sagittal specimens) than both control tissues (FWHM=$\sim$5 cm^{-1} for coronal no bead and empty bead specimens and $\sim$7 cm^{-1} for no bead and empty bead sagittal specimens). There is also a significant difference ($p < 0.01$) for the 945 cm^{-1} band in the coronal control bandwidths (FWHM=$\sim$7 cm^{-1}) and the coronal FGF2-treated bandwidths (FWHM=$\sim$9 cm^{-1}). In addition, the total integrated band area for the 945 cm^{-1} band in the FGF2-treated coronal sutures is greater (12.4$\pm$1.0) than the FGF2-treated sagittal sutures (10.3$\pm$1.4).

4 Discussion

The genetic basis of certain craniosynostosis gene mutations is increasingly well understood. However, the resulting chemical composition changes are not well understood. There is a great need to understand the precise chemical changes that are the first indication that a suture is undergoing cranio-
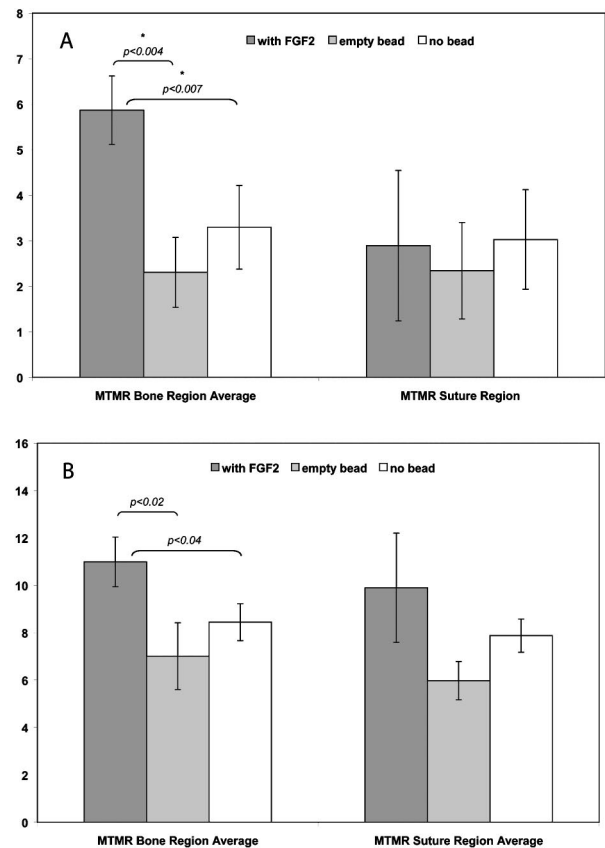
synostosis. For this reason we have chosen Raman spectroscopy to monitor the changes within craniosynostotic tissue. In this study, Raman microspectroscopic imaging provides chemical information about normal and craniosynostotic tis-
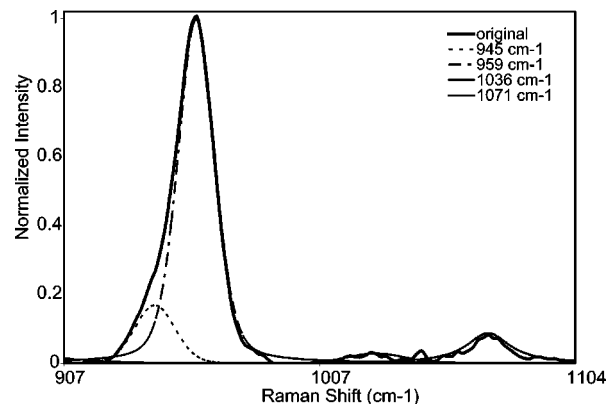

Fig. 6 Raman mineral factor with underlying bands. Curve fitting shows the two main bands that produce the ν_1 PO$_4^{3-}$ envelope of the bone mineral, 945 and 958 cm^{-1}. The ν_1 CO$_3^{2-}$ band is symmetric and modeled by a single band.
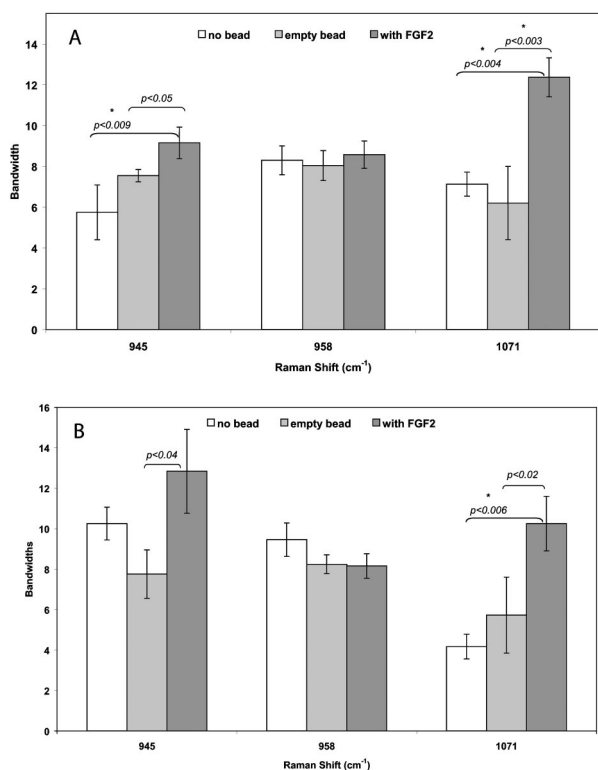
Fig. 7 Bandwidth comparison of the mineral bands at 945, 958, and 1071 cm^{-1}. The 945 cm^{-1} band most closely resembles that of a disordered calcium phosphate while the 958 cm^{-1} band is indicative of a stoichiometric hydroxyapatite. The 1071 cm^{-1} band corresponds to a type-B carbonated hydroxyapatite. There is an increase in the bandwidth of the 945 cm^{-1} band in the FGF2-treated coronal suture as well as an increase in the bandwidth of the 1071 cm^{-1} band compared to the no bead and empty bead coronal sutures (A). In the sagittal suture, the FGF2-treated sutures show an increase in the bandwidth of the 1071 cm^{-1} band (B). The asterisks indicate where $p < 0.01$.

sue that has not been previously available. Here we characterize the mineral and discuss possible mechanisms for FGF2-induced craniosynostosis.

Specimens treated with no bead and empty beads were used as controls in our work. In our study, parameters such as the MTMRs are not significantly different for no bead and empty bead specimens in either the sagittal ($p > 0.14$) or coronal sutures ($p > 0.19$). In the control suture specimens, the MTMRs did not vary significantly between the bone region and the suture region. Previous studies have shown no significant difference in osteonectin or alkaline phosphatase production[42] and bone morphogenetic protein 2 (BMP2) and TWIST expression[43] between the sutural regions of no bead and empty bead specimens.

The average bone region and suture region MTMRs for the no bead coronal were 3.29 ± 0.92 and 3.03 ± 1.09, respectively, while the empty bead coronal bone region average and suture region MTMRs were 2.30 ± 0.77 and 2.34 ± 1.06, respectively. Similar results were obtained for the sagittal suture specimens with the average bone region and suture region MTMRs for the no bead sagittal were 8.44 ± 0.51 and 7.88 ± 1.93, respectively, while the empty bead sagittal average bone region and suture region MTMRs were 7.01 ± 1.10 and

5.97 ± 0.32, respectively. These results confirm the validity of no bead and empty bead specimens as controls.

There is a significant difference between the MTMRs of the bone and suture regions of FGF2-treated specimens, as shown in Fig. 4. The combined coronal suture control mean MTMR is 2.80 ± 0.70 for the bone region and 2.69 ± 0.49 for the suture region. The MTMR for the FGF2-treated coronal suture bone region is 5.87 ± 0.75, more than $2\times$ greater than that of the control coronal bone region MTMR [Fig. 5(A)]. The results for the sagittal suture bone region MTMRs [Fig. 5(B)] show similar trends. However, the average FGF2-treated sagittal suture bone region MTMR is 10.99 ± 0.63, less than $1.5\times$ the control sagittal suture bone region MTMRs. These results are consistent with our previous work in which coronal sutures were found to be more likely to fuse and overlap and exhibited higher Msx2 expression than posterior frontal or sagittal sutures following FGF2 treatment.[18] This is also evidence that the principal site of action for FGF2-induced craniosynostosis is the osteogenic fronts, or the tips of the bones, and not the cells within the suture.

Unlike the averaged bone region MTMR, the averaged suture region MTMRs show no significant difference between control sutures and FGF2-treated sutures ($p > 0.64$, coronal, and $p > 0.07$, sagittal). This finding also is explained by the short duration of the tissue culture. Iseki, Wilkie, Morriss-Kay demonstrate a delayed mineralization around the site of the bead within the 48 h time period, but FGF2 requires only 2 h to reach the skeletogenic membrane.[42] Thus, we would not expect to see increased mineralization in the suture region unless the sutures have been cultured longer than 48 h.

It is apparent that there is no increased mineralization in the suture region of the coronal or sagittal sutures. We find that increased mineralization appears to occur in the bone region. Histology has not been able to confirm the type of mineral present in the areas of increased mineralization. The increased phosphate bandwidths in the Raman spectra of the FGF2-soaked tissue compared to the controls indicate that the rapid deposition of mineral results in a low crystallinity mineral, similar to that observed in other bone mineralization studies.[44]

Bandwidths are used as a measure of size and order in the crystal lattice of minerals. As a crystal lattice becomes larger and less disordered the bandwidth decreases.[45] Figure 6 shows the bands used to fit the Raman mineral factors. The most prominent band in the bone Raman spectrum is the v_1 PO_4^{3-} stretch at 959 cm^{-1}, in this case corresponding to a carbonated apatite. The band is broader on the low wave number side than on the high wave number side. The asymmetry is caused by an incompletely resolved band at 945 cm^{-1}, indicative of a disordered calcium phosphate. The other prominent band of interest in the Raman mineral spectrum is the v_1 CO_3^{2-} band at 1071 cm^{-1}. The carbonate band is more symmetric and can be modeled by only a single band. The 945 cm^{-1} component of the phosphate band is responsible for the increased width in the spectra of FGF2-treated specimens. The intense carbonated apatite band component at 958 cm^{-1} is no broader in the FGF2-treated specimens than in the controls. The 1071 cm^{-1} carbonate band is also broadened in the FGF2-treated specimens. The 1036 cm^{-1} band, v_3 PO_4^{3-}, is

not of interest in this study but is included in the fits for completeness.

Mineralization occurs more rapidly in the FGF2-treated coronal suture compared to the FGF2-treated sagittal suture. Consistent with the presence of more newly deposited mineral in the coronal suture specimens, the disordered phosphate 945 cm^{-1} band broadens more than the band in the sagittal suture specimens. Similarly, the integrated intensity (area) of the 945 cm^{-1} band relative to the 958 cm^{-1} band is greater in the FGF2-treated coronal sutures. This observation is another indication of the greater abundance of recently deposited mineral.

5 Summary

In conclusion, Raman microspectroscopic imaging has provided new information about the chemical composition brought about by FGF2-induced craniosynostosis. The mineral in the craniosynostotic tissue is comparable to the mineral in normal fetal day 18.5 tissue but exhibits increased amounts of mineral. Thus, the genetic mutations do not necessarily stimulate a different mineralization mechanism, merely an accelerated one resulting in a less ordered mineral structure.

References

1. N. H. Robin, "Molecular genetic advances in understanding craniosynostosis," *Plast. Reconstr. Surg.* **103**(3), 1060–1070 (1999).
2. E. W. Jabs, "Toward understanding the pathogenesis of craniosynostosis through clinical and molecular correlates," *Clin. Genet.* **53**, 79–86 (1998).
3. M. M. Cohen and R. MacLean, *Craniosynostosis*, Oxford University Press, New York (2000).
4. F. L. McIntyre, "Craniosynostosis," *Am. Fam. Physician* **55**(4), 1173–1178 (1997).
5. F. Bronner and M. Farrach-Carson, *Bone Formation*, Springer, New York (2004).
6. J. Davies, *The Bone-Biomaterial Interface*, University of Toronto Press, Toronto, Ontario (1991).
7. L. A. Opperman, "Cranial sutures as intramembranous bone growth sites," *Dev. Dyn.* **219**, 472–485 (2000).
8. W. Ozaki, S. R. Buchman, K. M. Muraszko, and D. Coleman, "Investigation of the influences of biomechanical force on the ultrastructure of human sagittal craniosynostosis," *Plast. Reconstr. Surg.* **102**(5), 1385–1394 (1998).
9. A. O. Wilkie, "Craniosynostosis: genes and mechanisms," *Hum. Mol. Genet.* **6**(10), 1647–1656 (1997).
10. M. Muenke, K. W. Gripp, D. M. McDonald-McGinn, K. Gaudenz, L. A. Whitaker, S. P. Bartlett, R. I. Markowitz, N. H. Robin, N. Nwokoro, J. J. Mulvihill, H. W. Losken, J. B. Mulliken, A. E. Guttmacher, R. S. Wilroy, L. A. Clarke, G. Hollway, L. C. Adès, E. A. Haan, J. C. Mulley, M. M. Cohen, Jr., G. A. Bellus, C. A. Francomano, D. M. Moloney, S. A. Wall, A. O. K. Wilkie, and E. H. Zachai, "A unique point mutation in the fibroblast growth factor receptor 3 gene (FGFR3) defines a new craniosynostosis syndrome," *Am. J. Hum. Genet.* **60**, 555–564 (1997).
11. B. Mehrara, D. Most, J. Chang, S. Bresnick, A. Turk, S. Schendel, G. Gittes, and M. Longaker, "Basic fibroblast growth factor and transforming growth factor β-1 expression in the developing dura mater correlates with calvarial bone formation," *Plast. Reconstr. Surg.* **104**(2), 435–444 (1999).
12. A. Lomri, J. Lemonnier, M. Hott, N. de Parseval, E. Lajeunie, A. Munnich, D. Renier, and P. J. Marie, "Increased calvaria cell differentiation and bone matrix formation induced by fibroblast growth factor receptor 2 mutations in Apert syndrome," *J. Clin. Invest.* **101**(6), 1301–1317 (1998).
13. Y.-H. Liu, Z. Tang, R. K. Kundu, L. Wu, W. Luo, D. Zhu, F. Sangiorgi, M. L. Snead, and R. E. Maxson, Jr., "Msx2 gene dosage influences the number of proliferative osteogenic cells in growth centers of the developing murine skull: A possible mechanism for Msx2-mediated craniosynostosis in humans," *Dev. Biol.* **205**, 260–274 (1999).
14. F. S. Kaplan, W. C. Hayes, T. M. Keaveny, A. Boskey, T. A. Einhorn, and J. P. Iannotti, *Form and Function of Bone*, Chap. 4, pp. 127–184, American Academy of Orthopaedic Surgeons, Rosemont, IL (1994).
15. Y. H. Liu, R. Kundu, L. Wu, W. Luo, M. A. Ignelzi, Jr., M. L. Snead, and R. E. Maxson, Jr., "Premature suture closure and ectopic cranial bone in mice expressing Msx2 transgenes in the developing skull," *Proc. Natl. Acad. Sci. U.S.A.* **92**, 6137–6141 (1995).
16. J. A. Greenwald, B. J. Mehrara, J. A. Spector, S. M. Warren, P. J. Fagenholz, L. P. Smith, P. J. Bouletreau, F. E. Crisera, H. Ueno, and M. T. Longaker, "In vivo modulation of FGF biological activity alters cranial suture fate," *Am. J. Pathol.* **158**(2), 441–452 (2001).
17. A. M. Moursi, P. L. Winnard, A. V. Winnard, J. M. Rubenstrunk, and M. P. Mooney, "Fibroblast growth factor 2 induces calvarial osteoblast proliferation and cranial suture fusion," *Cleft Palate Craniofac J.* **39**(5), 487–496 (2002).
18. M. A. Ignelzi, Jr., W. Wang, and A. T. Young, "Fibroblast growth factors lead to increased Msx2 expression and fusion in calvarial sutures," *J. Bone Miner. Res.* **18**(4), 751–759 (2003).
19. C. P. Tarnowski, M. A. Ignelzi, and M. D. Morris, "Mineralization of developing mouse calvaria as revealed by Raman microspectroscopy," *J. Bone Miner. Res.* **17**(6), 1118–1126 (2002).
20. D. Magne, P. Weiss, J.-M. Bouler, O. Laboux, and G. Daculsi, "Study of the maturation of the organic (type I collagen) and mineral (nonstoichiometric apatite) constituents of a calcified tissue (dentin) as a function of location: A Fourier Transform infrared microspectroscopic investigation," *J. Bone Miner. Res.* **16**(4), 750–757 (2001).
21. S. J. Gadaleta, N. P. Camacho, R. Mendelsohn, and A. L. Boskey, "Fourier Transform Infrared microscopy of calcified turkey leg tendon," *Calcif. Tissue Int.* **58**, 17–23 (1996).
22. R. Mendelsohn, A. Hassankhani, E. DiCarlo, and A. Boskey, "FT-IR microscopy of endochondral ossification at 20 m spatial resolution," *Calcif. Tissue Int.* **44**, 20–24 (1989).
23. J. Timlin, A. Carden, M. D. Morris, R. M. Rajachar, and D. H. Kohn, "Raman spectroscopic imaging markers for fatigue-related microdamage in bovine bone," *Anal. Chem.* **72**(10), 2229–2236 (2000).
24. L. A. Evans and R. Alvarez, "Characterization of the calcium biomineral in the radular teeth of Chiton pelliserpentis," *J. Bioinorg. Chem.* **4**, 166–170 (1999).
25. M. T. Kirchner, H. G. M. Edwards, D. Lucy, and A. M. Pollard, "Ancient and modern specimens of human teeth: A Fourier Transform Raman spectroscopic study," *J. Raman Spectrosc.* **28**, 171–178 (1997).
26. Smith and I. Rehman, "Fourier transform Raman spectroscopic studies of human bone," *Jugosl Ginekol Perinatol* **5**, 775–778 (1995).
27. O. Akkus, A. Polyakova-Akkus, F. Adar, and M. Schaffler, "Aging of microstructural compartments in human compact bone," *J. Bone Miner. Res.* **18**(6), 1012–1019 (2003).
28. N. Crane, W. Wang, M. Ignelzi, Jr., and M. Morris, "Spectral imaging of mouse skulls undergoing craniosynostosis," *Proc. SPIE* **4959**, 111–119 (2003).
29. A. L. Boskey, N. P. Camacho, R. Mendelsohn, S. B. Doty, and I. Binderman, "FT-IR microscopic mappings of early mineralization in chick limb bud mesenchymal cell cultures," *Calcif. Tissue Int.* **51**, 443–448 (1992).
30. E. P. Paschalis, E. DiCarlo, F. Betts, P. Sherman, R. Mendelsohn, and A. L. Boskey, "FTIR microspectroscopic analysis of human osteonal bone," *Calcif. Tissue Int.* **59**, 480–487 (1996).
31. N. P. Camacho, P. West, P. A. Torzilli, and R. Mendelsohn, "FTIR microscopic imaging of collagen and proteoglycan in bovine cartilage," *Biopolymers* **62**, 1–8 (2000).
32. M. Fitzmaurice, "Principles and pitfalls of diagnostic test development: implications for spectroscopic tissue diagnosis," *J. Biomed. Opt.* **5**(2), 119–130 (2000).
33. L. Bonewald, S. Harris, J. Rosser, S. Dallas, N. Camacho, B. Boyan, and A. Boskey, "Von Kossa staining alone is not sufficient to confirm

that mineralization in vitro represents bone formation," *Calcif. Tissue Int.* **72**, 537-547 (2003).

34. M. Morris, N. Crane, L. Gomez, and M. Ignelzi, Jr., "Compatibility of staining protocols for bone tissue with Raman imaging," *Calcif. Tissue Int.* **74**, 86–94 (2004).

35. E. Widjaja, N. Crane, T. Chen, M. D. Morris, M. A. Ignelzi, Jr., and B. McCreadie, "Band-Target Entropy Minimization (BTEM) applied to hyperspectral Raman image data," *Appl. Spectrosc.* **57**(11), 1353–1362 (2003).

36. K. Sasaki, S. Kawata, and S. Minami, "Component analysis of spatial and spectral patterns in multispectral images. II. Entropy minimization," *J. Opt. Soc. Am. A* **6**(1), 73–79 (1989).

37. E. Widjaja, C. Li, W. Chew, and M. Garland, "Band-Target Entropy Minimization. A robust algorithm for pure component spectra recovery. Application to complex randomized mixtures of six components," *Anal. Chem.* **75**, 4499–4507 (2003).

38. B. G. Frushour and J. L. Koenig, "Raman scattering of collagen, gelatin, and elastin," *Biopolymers* **14**, 379–391 (1975).

39. G. Ramachandran, *Treatise on Collagen*, Academic, New York (1967).

40. A. Carden, R. M. Rajachar, M. D. Morris, and D. H. Kohn, "Ultra-structural changes accompanying the mechanical deformation of bone tissue: a Raman imaging study," *Calcif. Tissue Int.* **72**, 166–175 (2003).

41. P. Tarakeshwar and S. Manogaran, "Proline and hydroxyproline zwitterions-an ab initio study," *J. Mol. Struct.: THEOCHEM* **417**, 255–263 (1997).

42. S. Iseki, A. O. M. Wilkie, and G. M. Morriss-Kay, "Fgfr1 and Fgfr2 have distinct differentiation- and proliferation-related roles in the developing mouse skull vent," *Development* **126**, 5611–5620 (1999).

43. D. P. C. Rice, T. Åberg, Y.-S. Chan, Z. Tang, P. J. Kettunen, L. Pakarinen, R. E. Maxson, Jr., and I. Thesleff, "Integration of FGF and TWIST in calvarial bone and suture development," *Development* **127**, 1845–1855 (2000).

44. L. Kuhn, Y. Xu, C. Rey, L. Gerstenfeld, M. Grynpas, J. Ackerman, H. Kim, and M. Glimcher, "Structure, composition, and maturation of newly deposited calcium-phosphate crystals in chicken osteoblast cell cultures," *J. Bone Miner. Res.* **15**(7), 1301–1309 (2000).

45. K. Rogers and P. Daniels, "An x-ray diffraction study of the effects of heat treatment on bone mineral microstructure," *Biomaterials* **23**, 2577–2585 (2002).

46. M. A. Walters, Y. C. Leung, N. C. Blumenthal, R. Z. LeGeros, and K. A. Konsker, "A Raman and infrared spectroscopic investigation of biological hydroxyapatite," *J. Inorg. Biochem.* **39**, 193–200 (1990).

47. B. O. Fowler, M. Markovic, and W. E. Brown, "Octacalcium phosphate. 3. Infrared and Raman vibrational spectra," *Chem. Mater.* **5**, 1417–1423 (1993).